ORIGINAL RESEARCH ARTICLE

Microstructure and Mechanical Properties of CoCrFeNiSi$_x$ (x = 0, 0.25, 0.5, 0.75) High-Entropy Alloys Based on Powder Plasma Arc Additive Manufacturing

Jinle Luo, Jiankun Wang, Chuanchu Su, Yanfei Geng, and Xizhang Chen

CoCrFeNi high-entropy alloy (HEA) has the characteristics of high plasticity and low strength, which limit its application and development. In this study, a novel powder plasma arc additive manufacturing technique was used to prepare CoCrFeNiSi$_x$ (x = 0, 0.25, 0.5, 0.75) HEAs. By using scanning electron microscope, x-ray diffractometer, electron backscattered diffraction, hardness tester and tensile tester, we analyzed the effect of Si element on the phase structure, microscopic morphology, hardness and tensile properties. The results show that CoCrFeNiSi$_x$ HEAs are composed of face-centered cubic (FCC) structure and the second phase (rich Ni and Si). The volume fraction of the second phase increases significantly with increasing Si content, while the grain size of the alloy decreases. The addition of Si markedly improved the hardness (160-454 HV) and yield strength (165.38-354.43 MPa) of the alloys, but the formation of the precipitated phase led to a decline in elongation (55.87-1.43%). These results provide a systematic understanding of the phase formation and mechanical properties of CoCrFeNiSi$_x$ HEAs.

1. Introduction

Traditional alloys design strategies are usually based on one or two major components with minor elements added to enhance specific properties. Based on this ideology, Yeh et al (Ref 1) and Cantor et al (Ref 2) proposed multi-component high-entropy alloys (HEAs). HEAs are generally composed of four or more major elements and the atomic percentage of each major element ranges from 5% to 35%. According to reports, HEAs have high-entropy effect, lattice distortion effect, slow diffusion effect and cocktail effect, which lead to their unique solid solution structure (Ref 3, 4), excellent mechanical properties (Ref 5, 6), and better corrosion resistance (Ref 7, 8). Therefore, HEAs have received extensive attention from scholars and are regarded as potential application materials in engineering practice.

Strength and ductility are two fundamental mechanical properties for the development of new structural materials.

Jinle Luo and Jiankun Wang have equally contributed to this work.

Jinle Luo, Jiankun Wang, Chuanchu Su, Yanfei Geng, and Xizhang Chen, College of Mechanical and Electrical Engineering, Wenzhou University, Wenzhou 325035, China. Contact e-mail: chenxizhang@wzu.edu.cn.

CoCrFeNi is the common HEA with good ductility, but its low strength limits the engineering applications (Ref 9, 10). Therefore, improving the mechanical properties of CoCrFeNi HEA has been the focus of current research. The strengthening mechanism of HEAs can be summarized as grain refinement strengthening, deformation strengthening, solid solution strengthening and precipitation strengthening. Post-treatment processes can promote the refinement of grain size and the formation of deformation twins, which can enhance the strength of the alloy (Ref 11, 12). Solid solution strengthening and precipitation strengthening are considered to be the most common strengthening methods in HEAs (Ref 13, 14). According to the research, the addition of large atomic radii can induce lattice distortion and the formation of second phases in HEAs (Ref 15-17). Recently, it has been shown that non-metallic elements with small atomic radii can also help to improve the microstructure and mechanical properties of HEAs (Ref 18, 19). Yang et al. (Ref 20) investigated the effects of C and Si on CoCrFeMn at different temperatures, and found that the deformation mechanism of the alloy would change from primary mechanical twinning to secondary nano-twining as the temperature decreased. Moreover, the element Si effectively promotes lattice distortion and reduces the stacking fault energy of the alloy (Ref 21). The fast cooling helps the FeCoNiAl$_{0.2}$-Si$_{0.2}$ HEA form uniform FCC structures and generate stable passivation films, leading to good corrosion resistance and soft magnetic properties (Ref 22).

At present, the main manufacturing methods for HEAs are vacuum arc melting and casting. These two processes have the disadvantages of the long production cycle and high production cost, which greatly limit the manufacture and production of HEAs. The rapid development of additive manufacturing (AM) technology provides a new option for the preparation of HEAs. AM technology features direct molding of complex-shaped products, controllable and adjustable local melt pools and

extremely fast cooling rates. AM uses lasers and electron beams as processing heat sources. It can be divided into selective laser melting (SLM) (Ref 23, 24), direct laser deposition (DLD) (Ref 25, 26) and selective electron beam melting (SEBM) (Ref 27). In recent years, powder plasma arc additive manufacturing (PPA-AM) has begun to be applied to HEAs. Compared to SLM, PPA-AM has a very high prospect for commercial applications. PPA-AM not only has the advantage of high deposition efficiency and low equipment cost, but also has a very wide range of applications due to its higher processing temperature (Ref 28, 29).

In this work, CoCrFeNiSi$_x$ (x = 0, 0.25, 0.5, 0.75) HEAs were fabricated by PPA-AM. The effects of Si on the microstructure and mechanical properties of CoCrFeNi HEA were systematically discussed. This paper provides a reference for the preparation of CoCrFeNiSi$_x$ HEAs with excellent mechanical properties using PPA-AM technology, while promoting the practical application of HEAs in industry.

2. Materials and Methods

In this experiment, CoCrFeNiSi$_x$ (x = 0, 0.25, 0.5, 0.75) HEAs samples were prepared by using Co, Cr, Fe, Ni, and Si powders (purity ≥ 99.5%, 150-250 mesh). Named as Si$_0$, Si$_{0.25}$, Si$_{0.5}$, Si$_{0.75}$, respectively. After the powders were weighed in molar ratio, powders and Al$_2$O$_3$ grinding balls (the mass ratio of powders and grinding balls was 1:2) were put into a high energy ball mill (YXQM12L, MITR Ltd., Hunan, China) to mix for 3 hours. In addition, argon was used as the protective gas for powder mixing. After mixing well, the powders were put into a vacuum drying oven to dry for 2 hours. To ensure the accuracy of the experiment, the 304 stainless steel substrate surface was cleaned with anhydrous ethanol and polished with an angle grinder. Figure 1(a) shows the deposition equipment (DML-VO3AD, Duomu Company, Shanghai, China), deposition principle and deposition path for PPA-AM. The main manufacturing parameters of PPA-AM technology for CoCrFeNiSi$_x$ HEAs samples are shown in Table 1. In order to ensure good bonding between the substrate and the HEAs, it is necessary to preheat the substrate with a current of 60 A and deposit the first layer with a current of 100 A.

The macroscopic physical map of the representative HEA sample is shown in Fig. 1(b). Figure 1(c) presents the schematic diagram of sampling for microstructure observation and mechanical property testing. The Instron universal material testing machine was used to conduct the tensile tests with a loading speed of 1.0 mm/min and the tensile specimen geometry is shown in Fig. 1(d). The Vickers hardness of the samples was measured using a Vickers hardness tester (HXS1000A) with a load of 9.8N and a delay time of 15 s. Three points at each position with a transverse distance of 1 mm were tested and the data were averaged. Phase compositions were determined by x-ray diffractometer (Bruker-D8-ADVANCE) using Cu Kα (λ = 1.5418 Å) at a scan speed of 5 °/min between 20° and 100°. Prior to XRD testing, the samples were sequentially sanded with 320 #, 600 #, 800 #, 1000 #, 1200 #, 1500 #, and 2000 # SiC sandpaper. Samples were corroded with aqua regia (HCL:HNO3 = 3:1). Scanning electron microscopy (SEM, Zeiss Sigma 300, Analytik Jena AG, Jena, Germany) and EDS (Oxford-X-MaxN-80) were used to observe the internal structure and elemental distribution of HEAs samples. The microstructure of HEAs was analyzed using electron backscatter diffraction (EBSD, Oxford Nordly Max3, Oxford Instrument Technology Co. Ltd.). The operating voltage of 20 kV and a step size of 8.0 μm (Si$_{0.25}$) and 0.4 μm (Si$_{0.75}$).

3. Result and Discussion

3.1 Microstructure Characteristics

Figure 2(a) shows the XRD patterns of the PPA-AM CoCrFeNiSi$_x$ (x = 0, 0.25, 0.5, and 0.75) HEAs. According to the XRD patterns, the Si$_0$ HEA exhibited a single FCC structure. With the addition of Si, the diffraction peaks of the second phase were detected in the Si$_{0.5}$ alloy. As for Si$_{0.75}$ alloys, the amount of diffraction peaks of the second phase increased significantly. It was indicated that the addition of Si could promote the generation of the second phase. The enlarged XRD patterns of the FCC$_{(111)}$ peak between 42° and 46° are shown in Fig. 2(b). Obviously, the diffraction peaks of FCC$_{(111)}$ in HEAs were shifted with the Si content. For x = 0 − 0.5, the diffraction peaks shifted gradually to the larger 2θ angle (43.812° to 43.931°). As the Si content reached 0.75, the diffraction peaks shifted toward a lower 2θ angle (43.780°). The lattice parameters of the FCC phase were calculated according to Bragg's Law. As shown in Fig. 2(c), the lattice constants of the FCC phase initially decrease and then increase, which are 3.5760, 3.5755, 3.5668 and 3.5785 Å, respectively. This trend can be attributed to the presence of Si. When the Si content is low, Si with smaller atomic radii (Co (125.10 pm), Cr (124.91 pm), Fe (124.12 pm), Ni (124.59 pm) and Si (115.30 pm)) was dissolved in the CoCrFeNi matrix, resulting in lattice shrinkage and decrease in lattice parameters (Ref 30). The phenomenon was similar to that of AlCoCrFeNiSi$_x$ (Ref 31). However, when the Si content is too excessive, Si is present as a second phase in the CoCrFeNi matrix, which leads to lattice distortion and an increase in the lattice parameters (Ref 32).

Figure 3 shows the microstructure of the CoCrFeNiSi$_x$ HEAs prepared by PPA-AM. The corresponding chemical compositions of the different regions of the PPA-AM CoCrFeNiSi$_x$ HEAs are summarized in Table 2. It can be seen from Fig. 3(a) that the CoCrFeNi-HEA prepared by the PPA-AM technique exhibits typical columnar crystallites. The formation of columnar crystals may be due to the rapid cooling and repeated thermal cycling during the processing of the AM technology. As shown in Fig. 3(b), the grain morphology of Si$_{0.25}$ HEA did not change significantly after the addition of Si (size about 94 μm). The alloy also did not generate a significant precipitation phase. It indicated that the Si in Si$_{0.25}$ HEA existed mainly in the alloy in the solid solution state. In the Si$_{0.5}$ HEA, the precipitated phase was clearly observed in Fig. 3(c). The morphology of the precipitated phase was mainly drop-like, and the elements were rich in Ni and Si (Fig. 4). It was further observed that the precipitated phase changed in the Si$_{0.75}$ HEA, showing irregular shapes crossing each other indicated in Fig. 3(d).

Zhang et al. (Ref 33) proposed the $\Delta H_{mix} - \delta$ criterion, combining the three parameters of mixing entropy (ΔS_{mix}), mixing enthalpy (ΔH_{mix}) and atomic size difference (δ) to
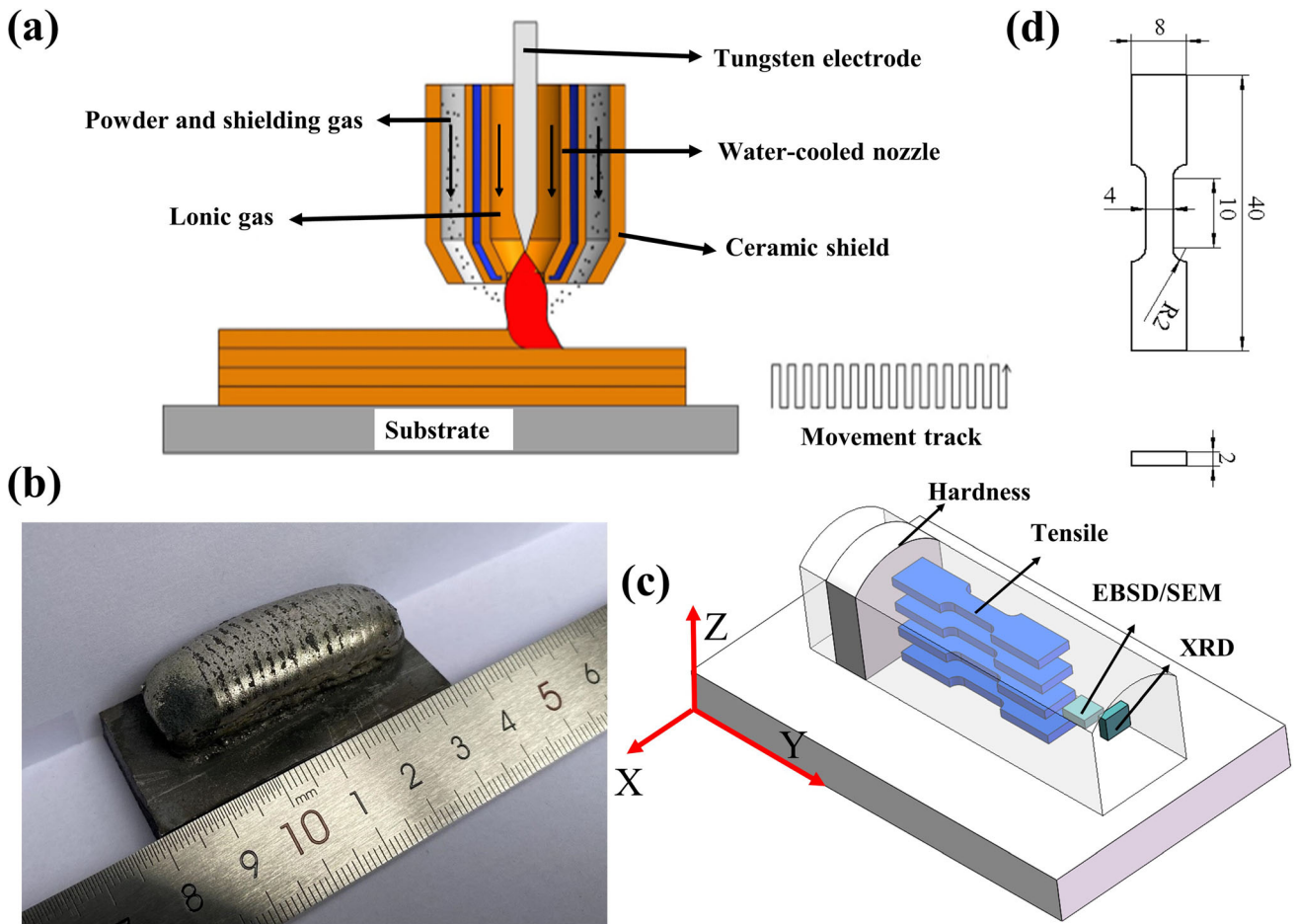
Fig. 1 (a) Schematic diagram of high-entropy alloys fabricated by PPA-AM, (b) as-deposited HEA blocks, (c) schematic showing the location of samples taken for microstructural evaluation, (d) the dimension of the tensile samples

Table 1 Key parameters of CoCrFeNiSi$_x$ HEAs Sample by PPA-AM Technology

Parameter	Value
Substrate thickness	10, mm
Torch and substrate distance	$10^{-1}5$, mm
Shield gas	15-20, L/min
Powder feeding gas	5, L/min
Preheating current	60, A
Deposition current	First layer 100 A, the other layers 60 A
Powder-feeding rotor speed	30, r/min
Wait time between layer	3, min
Layer thickness	2.5, mm
Travel speed	25, mm/min

predict the phases formation of HEA, which was expressed as follows:

$$\Delta S_{mix} = -R \sum_{i=1}^{n}(c_i ln c_i) \qquad (Eq\ 1)$$

$$\Delta H_{mix} = \sum_{i=1,i\neq j}^{n}(4\Delta H_{ij}^{mix}c_i c_j) \qquad (Eq\ 2)$$

$$\delta = \sqrt{\sum_{i=1}^{n} c_i \left(1 - \frac{r_i}{\bar{r}}\right)^2} \qquad (Eq\ 3)$$

Where R = 8.3144 J K^{-1} mol^{-1} is the molar gas constant, c_i and c_j are the atomic percentages of the i-th and j-th elements, respectively. ΔH_{ij}^{mix} is the mixing enthalpy between i-th element and j-th element and $\bar{r} = \sum_{i=1}^{n} c_i r_i$ is the average atomic radius. Table 3 showed the relevant parameters of HEAs, which are calculated based on Eq. 1, 2, and 3. These results are shown in Table 4.

The $\Delta H_{mix} - \delta$ criterion is used for HEAs with ΔS_{mix} between 12 and 17.5 J K^{-1} mol^{-1}. It can be seen from Table 4 that the ΔS_{mix} of Si$_{0.25}$, Si$_{0.5}$ and Si$_{0.75}$ in this experiment all meet the requirements of the $\Delta H_{mix} - \delta$ criterion. According to the $\Delta H_{mix} - \delta$ criterion, HEAs is more likely to form a solid solution in the range of $\delta < 6.5\%$ and -15 KJ mol$^{-1} < \Delta H_{mix} < 5$ KJ mol^{-1}. Beyond this range, the alloys is more inclined to form metallic compounds. As can be seen from Table 4, the δ values in this experiment were all less than 6.5%, which was consistent with the conditions for the formation of solid solution of the alloys. However, the ΔH_{mix} showed different results as the Si content increased. In this system, the negative ΔH_{mix} values between Si and the other metal elements are the largest, resulting in the ΔH_{mix} values of the HEAs decreasing significantly with the addition of Si. The ΔH_{mix} of
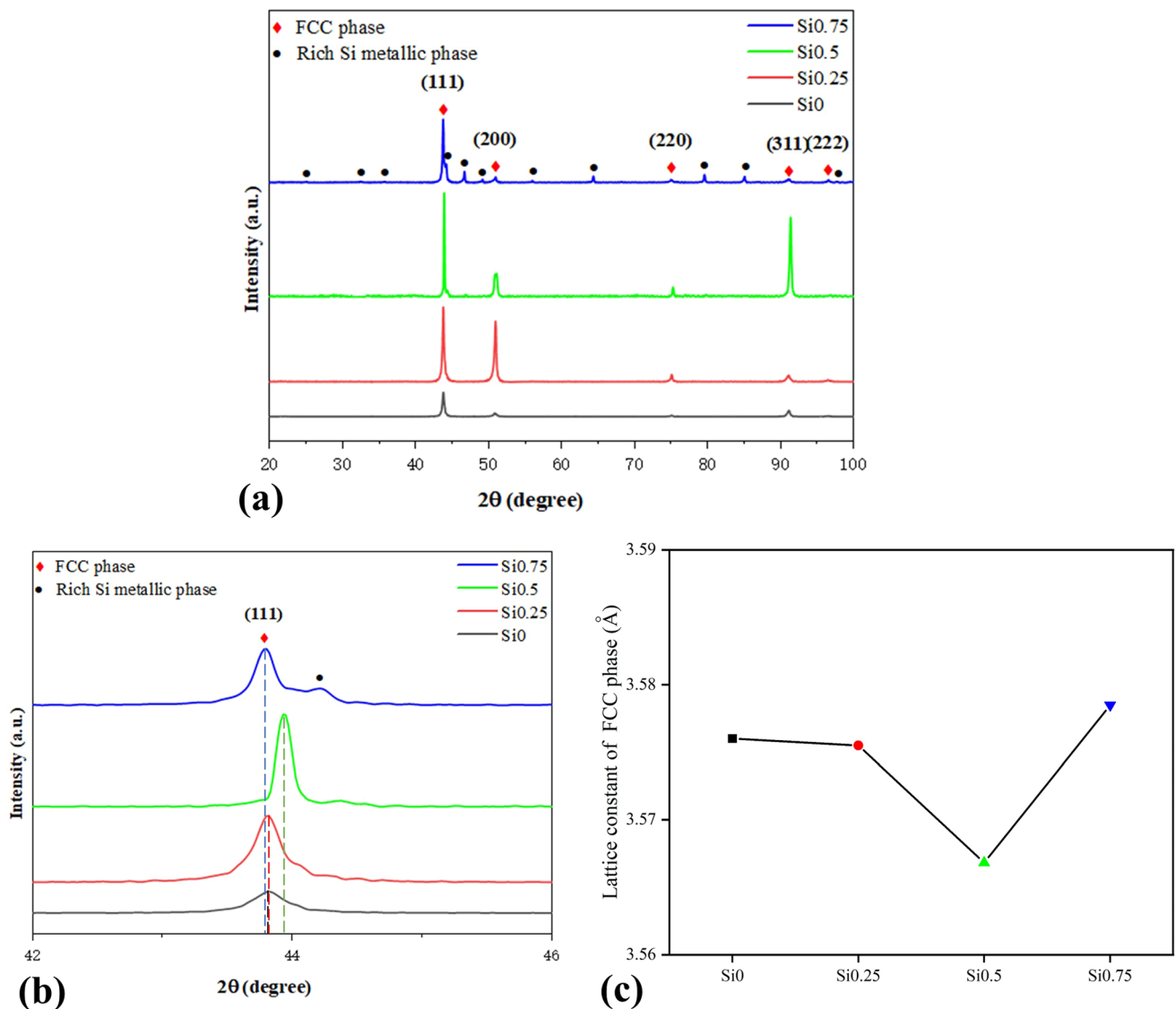
Fig. 2 (a) XRD patterns of CoCrFeNiSi$_x$ HEAs, (b) was the magnified images of the local diffraction peaks of (a), (c) lattice constants of FCC phase with increasing Si content

Si$_{0.25}$ is -11.46 KJ mol^{-1}, indicating that the alloy tends to a solid solution structure. With the further increased of Si content, the ΔH_{mix} of the alloys exceeded this range, at which point the alloys were more inclined to form metallic compounds. According to SEM (Fig. 3 and 4) and EDS (Table 2), the most metallic compounds (rich Ni and Si) were observed in Si$_{0.75}$ alloy. Si$_{0.75}$ alloy had the most negative mixing enthalpy, which made it easier to form metallic compounds. As well as more negative ΔH_{mix} between Ni and Si atoms to induce stronger interatomic bonding. Enriched Ni-Si phases were also observed in CoCrNiSi$_x$ (Ref 35) and CoFeNiSi$_x$ (Ref 36) HEAs. These results showed that $\Delta H_{mix} - \delta$ criterion is very suitable for predicting the effect of non-metallic element Si on the CoCrFeNi HEA system, and similar results are observed in CoCrFeNi-Si HEAs prepared by arc melting (Ref 32, 37).

To further analyze the phase composition of CoCrFeNiSi$_x$ HEAs, the representative samples Si$_{0.25}$ and Si$_{0.75}$ were characterized by EBSD. Figure 5 exhibits the EBSD phase maps of Si$_{0.25}$ and Si$_{0.75}$. Almost no precipitates were observed in Fig. 5(a). In contrast, up to 38.8% of precipitates were

detected in Si$_{0.75}$ HEA. It was consistent with the results of XRD and SEM. In addition, the grain size of Si$_{0.75}$ was smaller than Si$_{0.25}$. It was shown that the addition of Si not only promoted the generation of precipitated phases, but also refined the grain size of the alloy. For the Si$_{0.25}$ HEA, Si was mainly present in the alloy as solid solution. It led to the grain size similar to CoCrFeNi. On the other hand, the addition of large amounts of Si promoted the generation of precipitated phases in the alloy. The generated precipitates hinder the growth of the FCC matrix and refined the grain size of the alloy (Ref 35, 38).

The crystallographic orientations of Si$_{0.25}$ and Si$_{0.75}$ are shown in Fig. 6, including the inverse pole figures (IPFs) and pole figure (PFs). The IPF maps are indicated that Si$_{0.25}$ and Si$_{0.75}$ exhibit different crystal orientations. The Si$_{0.25}$ HEA exhibited random orientation, but the IPF map of Si$_{0.75}$ showed that the alloy tended to grow in the $< 111 >$ direction. There is no doubt that the crystal structure of the alloys has changed due to the addition of Si. The crystal structure of CoCrFeNi HEA prepared by PPA-AM tends to be $< 001 >$ (Ref 39, 40). The crystal structure of the alloy changed from $< 001 >$
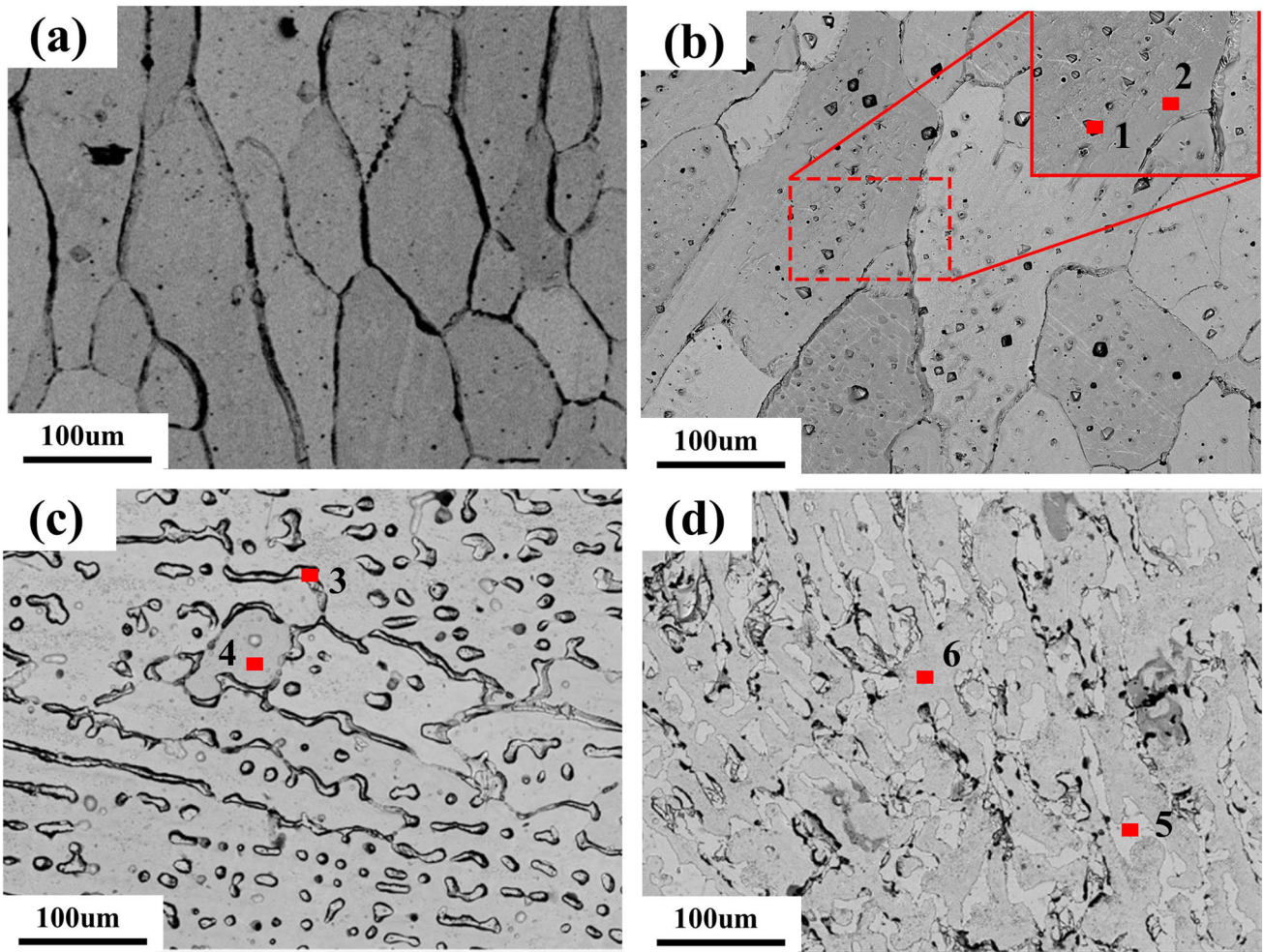
Fig. 3 Microstructure of CoCrFeNiSi$_x$ (x = 0, 0.25, 0.5, 0.75) HEAs by PPA-AM: (a) CoCrFeNi; (b) Si$_{0.25}$; (c) Si$_{0.5}$; (d) Si$_{0.75}$

Table 2 Elemental distribution of CoCrFeNiSi$_x$ (x = 0.25,0.5,0.75) HEAs at the marked area in Fig. 3. (wt.%)

Sample	Regions	Co	Cr	Fe	Ni	Si
Si$_{0.25}$	(1)	27.06	25.12	23.54	23.81	0.48
	(2)	26.59	20.48	24.39	27.02	1.52
Si$_{0.5}$	(3)	23.00	22.75	18.88	31.03	4.34
	(4)	27.11	19.96	26.16	25.17	1.59
Si$_{0.75}$	(5)	25.30	19.94	21.65	29.39	3.72
	(6)	27.05	20.01	25.91	24.71	2.31

to $<$ 111 $>$ with increasing Si content. In Fig. 6(c)-(f), it can be seen that the FCC phase exhibited different strong textures in Si$_{0.25}$ and Si$_{0.75}$. The FCC phase has a strong {100} texture in Si$_{0.25}$, but showed a strong {111} texture in Si$_{0.75}$. Meanwhile, Fig. 6(g) and (h) show the second phase PFs of Si$_{0.75}$, and the second has a strong {111} texture compared to the FCC phase (Fig. 6(e) and (f)). These evidences suggested that the crystal orientation in the alloy is similar to the single FCC structure when the Si content is lower (Ref 41). However, the FCC phase texture changed owing to the massive precipitation phase formation in HEA.

3.2 Mechanical Properties

Figure 7 shows the hardness of PPA-AM CoCrFeNiSi$_x$ (x = 0, 0.25, 0.5, 0.75) HEA. Apparently, the Si content has a significant effect on the hardness of the CoCrFeNiSi$_x$ alloy. The HEAs exhibited uniform hardness, indicating that the HEAs prepared by PPA-AM have a relatively uniform microstructure (Fig. 7(a)). As shown in Fig. 7(b), the average hardness of the alloys were 160.04 HV, 176.46 HV, 225.63 HV, 454.18 HV, respectively, indicating that the addition of Si significantly enhances the hardness of the alloys. In addition, the hardness from Si$_0$ to Si$_{0.25}$ is only increased by about 16 HV, while the hardness of Si$_{0.25}$ to Si$_{0.5}$ is increased by about 50 HV, indicating that the second phase is the main source of hardness enhancement of the alloys. Further when the Si content is increased up to Si$_{0.75}$, the hardness of the alloys increases substantially, but the hardness values show significant fluctuations. The fluctuation of hardness was attributed to the increase in the volume fraction of the second phase, which means that the hardness test points are on different phases, resulting in a difference in the hardness values.

Typical engineering strain-stress curves for CoCrFeNiSi$_x$ HEAs with different Si amounts are presented in Fig. 8. The yield strength (YS), ultimate tensile strength (UTS), and elongation to failure (EF) of CoCrFeNiSi$_x$ HEAs are summarized in Table 5. The results showed that the mechanical
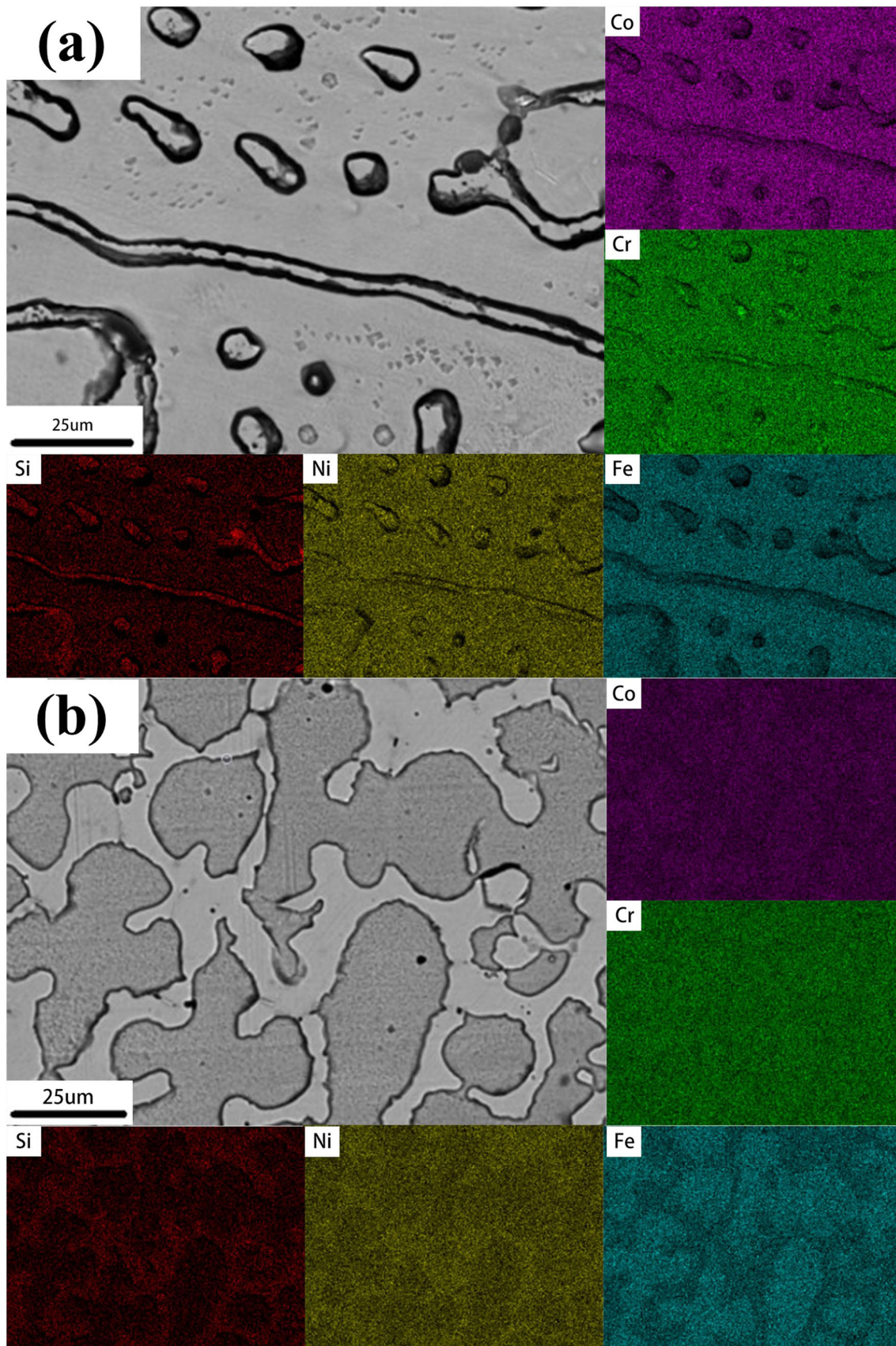
Fig. 4 EDS mappings of PPA-AM CoCrFeNiSi$_x$ HEAs (a) Si$_{0.5}$, (b) Si$_{0.75}$

properties of CoCrFeNi HEA prepared by PPA-AM technique were similar to those of as-cast (Ref 42). It shown that the preparation of HEAs by PPA-AM technology was feasible. With the increase of the Si content in CoCrFeNiSi$_x$ HEAs, the tensile strength of the alloy increases, while the plasticity decreases. The Si$_{0.25}$ HEA had a significantly increased YS of 302.43 MPa while the UTS increased to 604.68 MPa, and the EF reduced slightly (43.31%). When the Si content was increased to Si$_{0.5}$, YS increased to 305.02 MPa, but EF further decreased to 21.27%. As the Si content increased further, the YS and UTS of Si$_{0.75}$ alloy were 354.43 MPa and 425.89 MPa, respectively, but the EF was only 1.43%.

The mechanical properties variation depends on the different microstructures of CoCrFeNiSi$_x$. The addition of Si to the CoCrFeNi matrix induced lattice distortion of the FCC phase, leading to solid solution strengthening of the alloys. Secondly, the formation of the Si-rich precipitation phase significantly increased the hardness and strength of CoCrFeNiSi$_x$ alloys with the increasing Si content. Since metallic compounds often exhibit higher strength and lower plasticity than FCC phases. The second phase generated in this work is a hard intermetallic compound with a tetragonal structure (Ref 30). The hard second phases hinder dislocation motion but serves as a crack initiation during the tensile process. For Si$_{0.25}$ alloy, the higher strength and lower plasticity compared to CoCrFeNi HEA is attributed to the majority of the Si element being dissolved in the FCC matrix, with only trace amounts of point-like precipitated phases. However, in Si$_{0.5}$ alloy the number of second phases increases dramatically and some of the precipitated phases are transformed into continuous precipitated phases, leading to the increase in strength and decrease in ductility. Further at Si$_{0.75}$, the second phase is totally continuous in the FCC matrix, which greatly contributes to crack propagation during the tensile process, leading to embrittlement of the alloy. The continuous precipitation phase causes a decrease in tensile strength and plasticity (Ref 30, 39).

Figure 9 show the fracture morphologies of CoCrFeNiSi$_x$ HEAs after tensile deformation. As shown in Fig. 9(a) and (d), many microvoids and deep dimples can be seen in the fracture morphologies of the Si$_{0.25}$ alloy, which indicated that the alloy undergoes ductile fracture, corresponding to the higher plasticity (43.31%) in Fig. 8. With the increase of Si content, the alloy gradually transforms from ductile fracture to cleavage fracture. For the Si$_{0.5}$ alloy, microvoids and propagating cracks can be clearly observed in Fig. 9(b). The formation of metallic compounds made the alloy more prone to propagation cracks during stretching (Ref 43), and the generation of cracks will reduce the plasticity of the alloy. As seen in Fig. 9(e), the alloy exhibited partial dimples and smooth cleavage surfaces with many small cracks, which illustrates the fracture mode of the ductile and brittle mixture. With further increase of Si content, the tensile fracture surfaces of Si0.75 alloy showed the brittle fracture morphology with cleavage fracture in the continuous
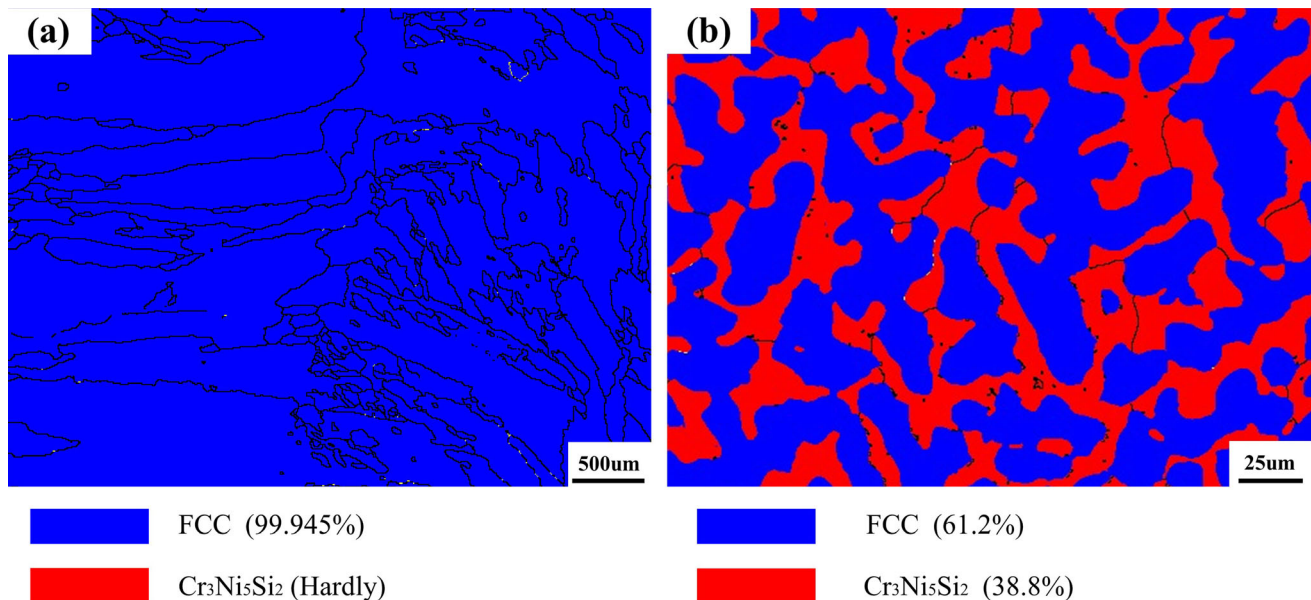
Table 3 Atomic radius and the enthalpy of binary mixing between elements (H_{ij}^{mix}) (Ref 34)

Element and Atomic radius, nm	Cr	Fe	Ni	Si
Co (0.12510)	− 4	− 1	0	− 38
Cr (0.12491)		− 1	− 7	− 37
Fe (0.12412)			− 2	− 35
Ni (0.12459)				− 40
Si (0.11530)				

Table 4 ΔS_{mix}, ΔH_{mix} and δ of the CoCrFeNiSi$_x$ (x = 0.25, 0.5, 0.75) HEAs

Alloys	ΔS_{mix}, J K^{-1} mol^{-1}	ΔH_{mix}, KJ mol^{-1}	δ, %
Si$_{0.25}$	12.72	− 11.46	1.80
Si$_{0.5}$	13.14	− 17.78	2.40
Si$_{0.75}$	13.30	− 22.60	2.79

(a) 500um

FCC (99.945%)

Cr$_3$Ni$_5$Si$_2$ (Hardly)

(b) 25um

FCC (61.2%)

Cr$_3$Ni$_5$Si$_2$ (38.8%)
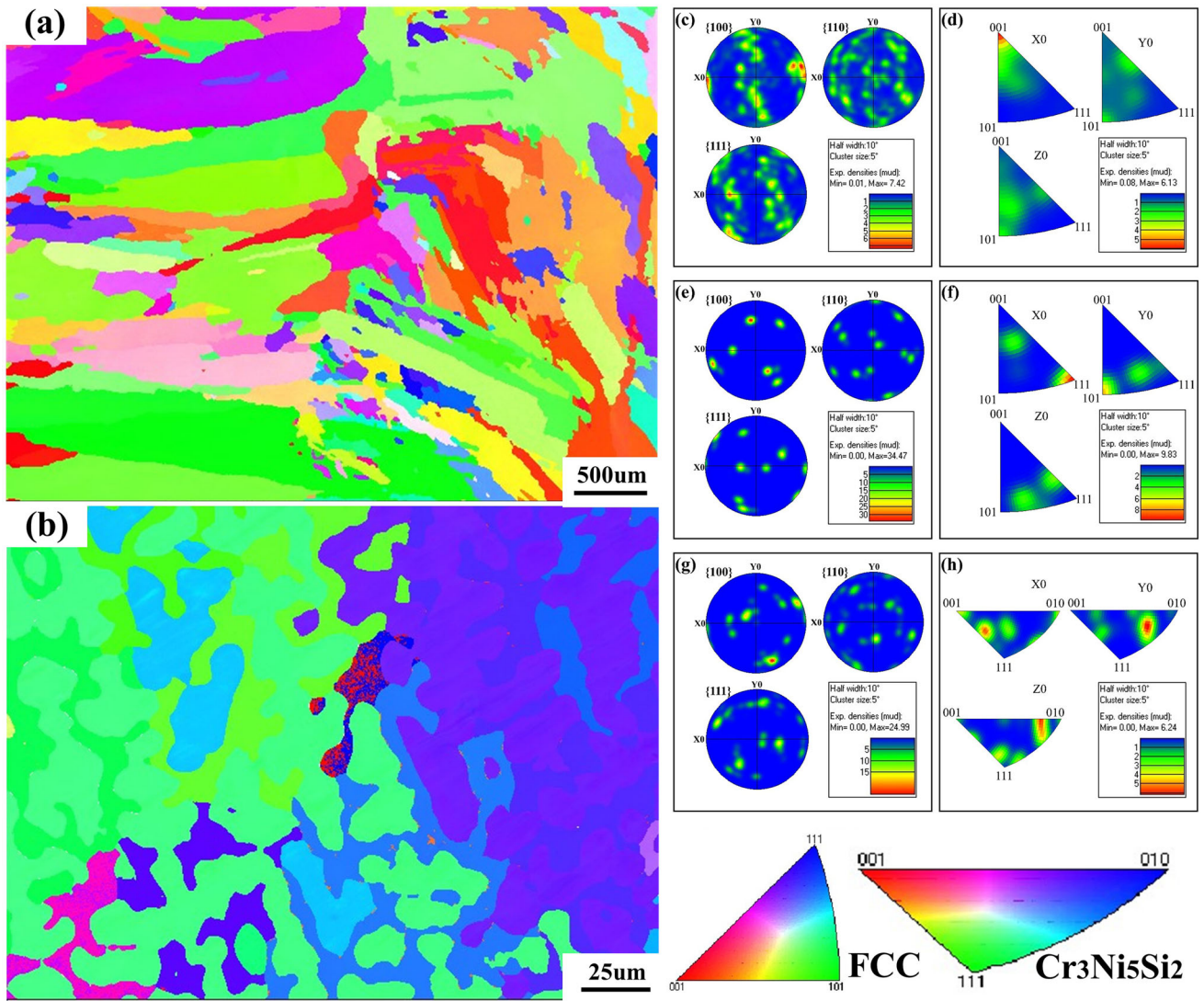
Fig. 5 EBSD phase maps of the HEAs: (a) Si$_{0.25}$, (b) Si$_{0.75}$

Fig. 6 IPFs and corresponding PFs for $Si_{0.25}$ and $Si_{0.75}$ alloys:(a), (c) and (d) $Si_{0.25}$; (b), (e), (f), (g) and (h) $Si_{0.75}$
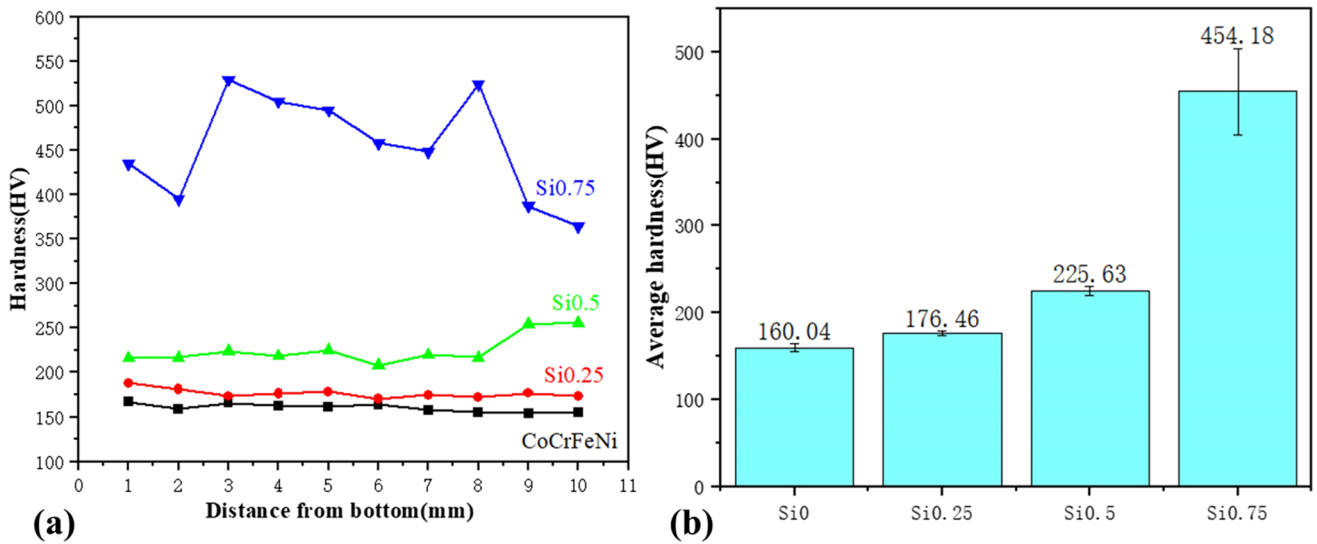

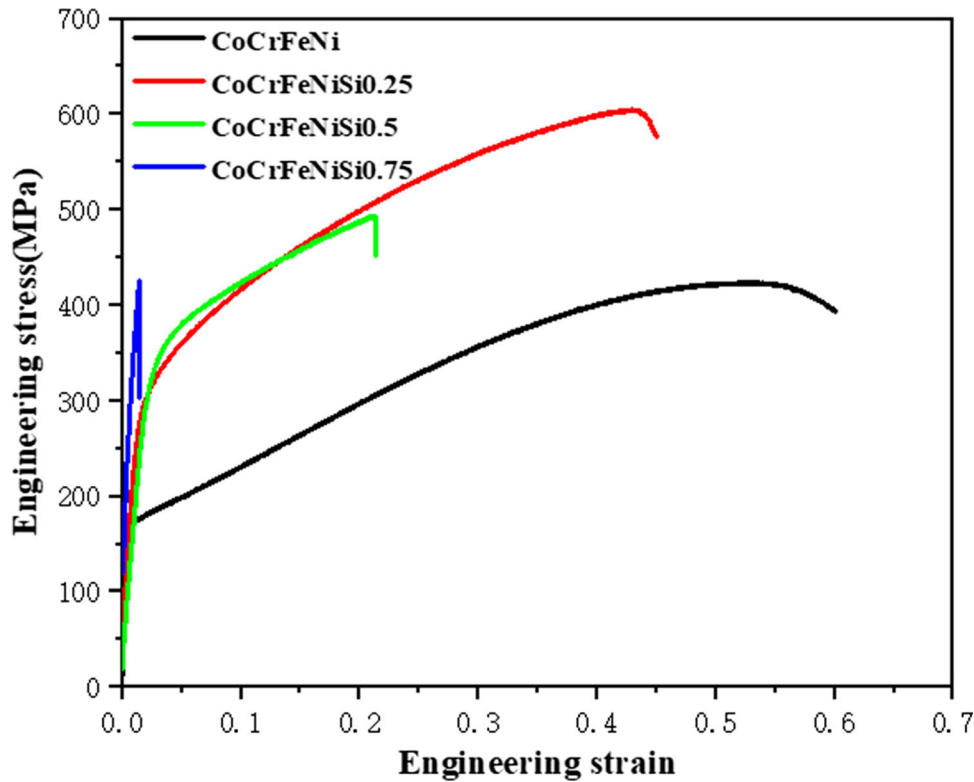**Fig. 7** (a) The hardness distribution of PPA-AM $CoCrFeNiSi_x$ HEAs samples;(b) The average hardness of each sample

Fig. 8 Engineering stress-strain curves of PPA-AM CoCrFeNiSi$_x$ (x = 0,0.25,0.5,0.75) HEAs at room temperature

Table 5 The yield strength (YS), ultimate tensile strength (UTS), and Elongation to failure (EF) (for the PPA-AM CoCrFeNiSi$_x$ (x = 0, 0.25, 0.5 and 0.75) alloys and as-cast CoCrFeNi (Ref 42)

Alloys	YS, MPa	UTS, MPa	EF, %
CoCrFeNi	165.38	420.01	55.87
CoCrFeNi(as-cast)	155.00	472.40	58.90
CoCrFeNiSi$_{0.25}$	302.43	604.68	43.31
CoCrFeNiSi$_{0.5}$	305.02	493.32	21.27
CoCrFeNiSi$_{0.75}$	354.43	425.89	1.43

precipitation phase as shown in Fig. 9(c) and (f). The cross section was very smooth with some irregularly curved pits and long cracks parallel to each other. The second phase in Si$_{0.75}$ had some ductile FCC phases internal to impede crack extension, but the massive and continuous Ni-Si precipitated phases promoted crack growth, which led to a substantial decrease ductility. These fracture mode features are consistent with the tensile properties of the CoCrFeNiSi$_x$ HEAs in this experiment.

4. Conclusion

In this work, a novel powder plasma arc additive manufacturing (PPA-AM) has been used to fabricate CoCrFeNiSi$_x$ (x = 0.25,0.5,0.75) HEAs. The phase evolution, strengthening mechanisms and fracture morphologies were investigated in PPA-AM CoCrFeNiSi$_x$ HEAs. The main conclusions of this study are as follows:

(1) CoCrFeNiSi$_x$ HEAs without obvious defects were successfully prepared via PPA-AM. The phase composition of the CoCrFeNiSi$_x$ high-entropy alloys consists of a face-centered cubic (FCC) structure and the second phase (rich in Ni and Si). With the increase of Si content, the microstructure of the second phase is transformed from FCC matrix precipitation to intersection with the matrix.

(2) As the Si content increases, the strong texture of the FCC phase in the alloy changes from {001} to {111}. The addition of Si significantly reduces the grain size of the face-centered cubic phase, which is mainly due to the formation of precipitated phases that inhibit the growth of the FCC phase.

(3) The addition of Si significantly increased the hardness (from 160 to 454 HV) and yield strength (from 165.38 to 354.43 MPa) of CoCrFeNiSi$_x$ HEAs, while the ductility decreased (from 55.87 to 1.43%). HEAs transition from ductile fracture to brittle fracture due to the increase in Si content, which is due to the brittle metallic compounds contributing to crack propagation. Si$_{0.25}$ exhibited excellent tensile strength-ductility synergy with the elongation of 43.3% and the tensile strength of 604 MPa, which was attributed to the solid solution strengthening.
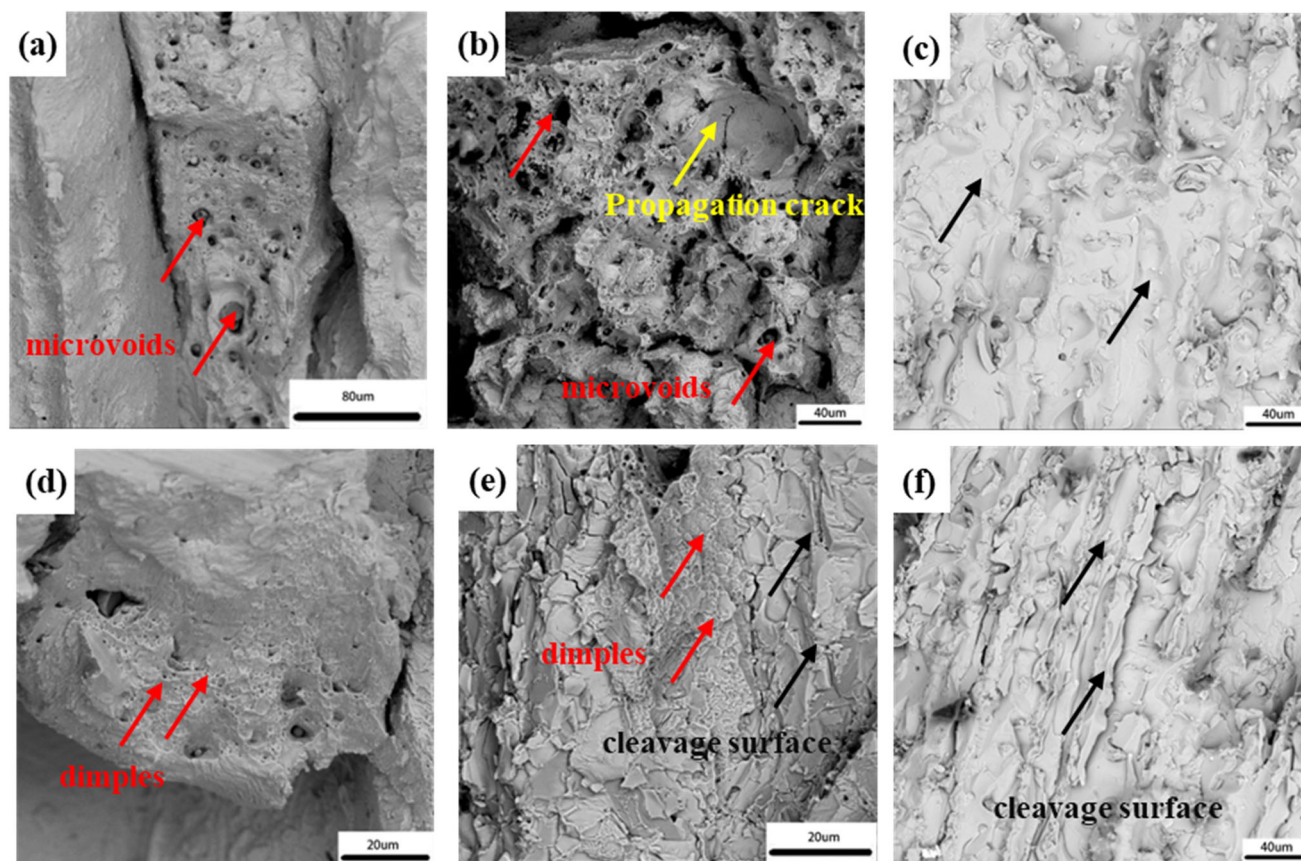
Fig. 9 Fracture morphologies of CoCrFeNiSi$_x$ HEAs: (a) and (d) Si$_{0.25}$; (b) and (e) Si$_{0.5}$; (c) and (f) Si$_{0.75}$

Author Contribution

JL: Conceptualization, Investigation, Methodology, Writing – original draft. JW: Supervision, Writing – review & editing. CS: Supervision. YG: Supervision. XC: Supervision, Funding acquisition.

Data and code Availability

The data that support the findings of this study are available from the corresponding author upon reasonable request.

Conflict of interest

The authors declare that they have no known competing financial interests or personal relationships that could have appeared to influence the work reported in this paper.

Ethical Approval

This study and included experiments have no ethical issues involved.

References

1. J.-W. Yeh, S.-K. Chen, S.-J. Lin, J.-Y. Gan, T.-S. Chin, T.-T. Shun, C.-H. Tsau, and S.-Y. Chang, Nanostructured High-Entropy Alloys with Multiple Principal Elements: Novel Alloy Design Concepts and Outcomes, *Adv. Eng. Mater.*, 2004, **6**(5), p 299–303.
2. B. Cantor, I.T.H. Chang, P. Knight, and A.J.B. Vincent, Microstructural Development in Equiatomic Multicomponent Alloys, *Mater. Sci. Eng., A*, 2004, **375–377**, p 213–218.
3. M. Vaidya, A. Anupam, J.V. Bharadwaj, C. Srivastava, and B.S. Murty, Grain Growth Kinetics in CoCrFeNi and CoCrFeMnNi High Entropy Alloys Processed by Spark Plasma Sintering, *J. Alloys Compd.*, 2019, **791**, p 1114–1121.
4. D. Xie, R. Feng, P.K. Liaw, H. Bei, and Y. Gao, Long-Term Tensile Creep Behavior of a Family of FCC-Structured Multi-Component Equiatomic Solid Solution Alloys, *Scripta Mater.*, 2022, **212**, p 114556.
5. J. Moon, E. Tabachnikova, S. Shumilin, T. Hryhorova, Y. Estrin, J. Brechtl, P.K. Liaw, W. Wang, K.A. Dahmen, A. Zargaran, J.W. Bae, H.-S. Do, B.-J. Lee, and H.S. Kim, Deformation Behavior of a Co-Cr-Fe-Ni-Mo Medium-Entropy Alloy at Extremely Low Temperatures, *Mater. Today*, 2021, **50**, p 55–68.
6. D.D. Zhang, J.Y. Zhang, J. Kuang, G. Liu, and J. Sun, The B2 Phase-Driven Microstructural Heterogeneities and Twinning Enable Ultrahigh Cryogenic Strength and Large Ductility in NiCoCr-Based Medium-Entropy Alloy, *Acta Mater.*, 2022, **233**, p 117981.
7. Y. Qiu, S. Thomas, M.A. Gibson, H.L. Fraser, and N. Birbilis, Corrosion of High Entropy Alloys, *NPJ Mater. Degrad.*, 2017, **1**(1), p 15.
8. P. Muangtong, A. Rodchanarowan, D. Chaysuwan, N. Chanlek, and R. Goodall, The Corrosion Behaviour of CoCrFeNi-x (x = Cu, Al, Sn) High Entropy Alloy Systems in Chloride Solution, *Corros. Sci.*, 2020, **172**, p 108740.
9. Z. Wu, H. Bei, F. Otto, G.M. Pharr, and E.P. George, Recovery, Recrystallization, Grain Growth and Phase Stability of a Family of

FCC-Structured Multi-Component Equiatomic Solid Solution Alloys, *Interlmetallics*, 2014, **46**, p 131–140.

10. Z. Wu, H. Bei, G.M. Pharr, and E.P. George, Temperature Dependence of the Mechanical Properties of Equiatomic Solid Solution Alloys with Face-Centered Cubic Crystal Structures, *Acta Mater.*, 2014, **81**, p 428–441.

11. Z. An, S. Mao, Y. Liu, H. Zhou, Y. Zhai, Z. Tian, C. Liu, Z. Zhang, and X. Han, Hierarchical Grain Size and Nanotwin Gradient Microstructure for Improved Mechanical Properties of a Non-Equiatomic CoCrFeMn-Ni High-Entropy Alloy, *J. Mater. Sci. Technol.*, 2021, **92**, p 195–207.

12. W. Zhao, J.-K. Han, Y.O. Kuzminova, S.A. Evlashin, A.P. Zhilyaev, A.M. Pesin, J. Jang, K.-D. Liss, and M. Kawasaki, Significance of Grain Refinement on Micro-Mechanical Properties and Structures of Additively-Manufactured CoCrFeNi High-Entropy Alloy, *Mater. Sci. Eng., A*, 2021, **807**, p 140898.

13. J.Y. He, H. Wang, H.L. Huang, X.D. Xu, M.W. Chen, Y. Wu, X.J. Liu, T.G. Nieh, K. An, and Z.P. Lu, A Precipitation-Hardened High-Entropy Alloy with Outstanding Tensile Properties, *Acta Mater.*, 2016, **102**, p 187–196.

14. K. Zhou, Z. Wang, F. He, S. Liu, J. Li, J. Kai, and J. Wang, A Precipitation-Strengthened High-Entropy Alloy for Additive Manufacturing, *Addit. Manuf.*, 2020, **35**, p 101410.

15. U. Hecht, S. Gein, O. Stryzhyboroda, E. Eshed, and S. Osovski, The BCC-FCC Phase Transformation Pathways and Crystal Orientation Relationships in Dual Phase Materials From Al-(Co)-Cr-Fe-Ni Alloys, *Front. Mater.*, 2020, **7**, p 287.

16. H.-C. Liu and C.-W. Tsai, Effect of Ge Addition on the Microstructure, Mechanical Properties, and Corrosion Behavior of CoCrFeNi High-Entropy Alloys, *Intermetallics*, 2021, **132**, p 107167.

17. G.A. Salishchev, M.A. Tikhonovsky, D.G. Shaysultanov, N.D. Stepanov, A.V. Kuznetsov, I.V. Kolodiy, A.S. Tortika, and O.N. Senkov, Effect of Mn and V on Structure and Mechanical Properties of High-Entropy Alloys Based on CoCrFeNi System, *J. Alloys Compd.*, 2014, **591**, p 11–21.

18. Z.H. Yin, X.W. Liu, N. Gao, S.R. Li, J.Q. Yao, Z.T. Fan, W.B. Zhang, and Y.Z. Wang, Grain Refinement of a NiCoFe Medium Entropy Alloy: Composition Design from Solute Interaction Perspective, *J. Alloys Compd.*, 2023, **951**, p 169966.

19. Z. He, N. Jia, H. Wang, H. Yan, and Y. Shen, Synergy Effect of Multi-Strengthening Mechanisms in FeMnCoCrN HEA at Cryogenic Temperature, *J. Mater. Sci. Technol.*, 2021, **86**, p 158–170.

20. F. Yang, L. Dong, L. Cai, X. Hu, and F. Fang, Mechanical Properties of FeMnCoCr High Entropy Alloy Alloyed with C/Si at Low Temperatures, *J. Alloys Compd.*, 2021, **859**, p 157876.

21. H. Chang, T.W. Zhang, S.G. Ma, D. Zhao, R.L. Xiong, T. Wang, Z.Q. Li, and Z.H. Wang, Novel Si-Added CrCoNi Medium Entropy Alloys Achieving the Breakthrough of Strength-Ductility Trade-Off, *Mater. Des.*, 2021, **197**, p 109202.

22. C. Chen, H. Zhang, Y. Fan, R. Wei, W. Zhang, T. Wang, T. Zhang, K. Wu, F. Li, S. Guan, and J. Jiang, Improvement of Corrosion Resistance and Magnetic Properties of FeCoNiAl0.2Si0.2 High Entropy Alloy via Rapid-Solidification, *Intermetallics*, 2020, **122**, p 106778.

23. P. Chen, S. Li, Y. Zhou, M. Yan, and M.M. Attallah, Fabricating CoCrFeMnNi High Entropy Alloy via Selective Laser Melting In-Situ Alloying, *J. Mater. Sci. Technol.*, 2020, **43**, p 40–43.

24. Y. Lu, X. Wu, Z. Fu, Q. Yang, Y. Zhang, Q. Liu, T. Li, Y. Tian, H. Tan, Z. Li, T. Wang, and T. Li, Ductile and Ultrahigh-Strength Eutectic High-Entropy Alloys by Large-Volume 3D Printing, *J. Mater. Sci. Technol.*, 2022, **126**, p 15–21.

25. D. Svetlizky, M. Das, B. Zheng, A.L. Vyatskikh, S. Bose, A. Bandyopadhyay, J.M. Schoenung, E.J. Lavernia, and N. Eliaz, Directed Energy Deposition (DED) Additive Manufacturing: Physical Characteristics Defects, Challenges and Applications, *Mater. Today*, 2021, **49**, p 271–295.

26. Z.U. Arif, M.Y. Khalid, and E. Ur Rehman, Laser-Aided Additive Manufacturing of High Entropy Alloys: Processes, Properties, and Emerging Applications, *J. Manufact. Process.*, 2022, **78**, p 131–171.

27. C. Körner, Additive Manufacturing of Metallic Components by Selective Electron Beam Melting—a Review, *Int. Mater. Rev.*, 2016, **61**(5), p 361–377.

28. Q. Li, X. Chen, X. Chen, A.N. Siddiquee, V.B. Deev, S. Konovalov, and M. Wen, Microstructure Evolution of Additively Manufactured CoCrFeNiAl0.4 High-Entropy Alloy under Thermo-Mechanical Processing, *J. Mater. Res. Technol.*, 2022, **16**, p 442–450.

29. B. Dong, Z. Wang, Z. Pan, O. Muránsky, C. Shen, M. Reid, B. Wu, X. Chen, and H. Li, On the Development of Pseudo-Eutectic AlCoCrFeNi2.1 High Entropy Alloy Using Powder-Bed Arc Additive Manufacturing (PAAM) Process, *Mater. Sci. Eng.: A*, 2021, **802**, p 140639.

30. X. Gao, Y. Chen, R. Chen, T. Liu, H. Fang, G. Qin, Y. Su, and J. Guo, Tailoring Formation and Proportion of Strengthening Phase in Non-Equiatomic CoCrFeNi High Entropy Alloy by Alloying Si Element, *Intermetallics*, 2022, **147**, p 107617.

31. J.M. Zhu, H.M. Fu, H.F. Zhang, A.M. Wang, H. Li, and Z.Q. Hu, Synthesis and Properties of Multiprincipal Component AlCoCrFeNiSi$_x$ Alloys, *Mater. Sci. Eng., A*, 2010, **527**(27–28), p 7210–7214.

32. L. Huang, X. Wang, F. Jia, X. Zhao, B. Huang, J. Ma, and C. Wang, Effect of Si Element on Phase Transformation and Mechanical Properties for FeCoCrNiSix High Entropy Alloys, *Mater. Lett.*, 2021, **282**, p 128809.

33. Y. Zhang, Y.J. Zhou, J.P. Lin, G.L. Chen, and P.K. Liaw, Solid-Solution Phase Formation Rules for Multi-Component Alloys, *Adv. Eng. Mater.*, 2008, **10**(6), p 534–538.

34. A. Takeuchi and A. Inoue, Classification of Bulk Metallic Glasses by Atomic Size Difference, Heat of Mixing and Period of Constituent Elements and Its Application to Characterization of the Main Alloying Element, *Mater. Trans.*, 2005, **46**(12), p 2817–2829.

35. H. Yi, M. Bi, K. Yang, and B. Zhang, Significant Improvement the Mechanical Properties of CoCrNi Alloy by Tailoring a Dual FCC-Phase Structure, *Materials*, 2020, **13**(21), p 4909.

36. T.T. Zuo, R.B. Li, X.J. Ren, and Y. Zhang, Effects of Al and Si Addition on the Structure and Properties of CoFeNi Equal Atomic Ratio Alloy, *J. Magn. Magn. Mater.*, 2014, **371**, p 60–68.

37. K.H. Kong, K.C. Kim, W.T. Kim, and D.H. Kim, Microstructural Features of Multicomponent FeCoCrNiSi$_x$ Alloys, *AM*, 2015, **45**(1), p 32–36.

38. J.Y. He, H. Wang, H.L. Huang, X.D. Xu, M.W. Chen, Y. Wu, X.J. Liu, T.G. Nieh, K. An, and Z.P. Lu, A Precipitation-Hardened High-Entropy Alloy with Outstanding Tensile Properties, *Acta Mater.*, 2016, **102**, p 187–196.

39. Q. Shen, Powder Plasma Arc Additive Manufacturing of CoCrFeNiWx High-Entropy Alloys_ Microstructure Evolution and Mechanical Properties, *J. Alloys Compd.*, 2022, **922**, p 166245.

40. Y. Zhang, Q. Shen, X. Chen, S. Jayalakshmi, R.A. Singh, S. Konovalov, V.B. Deev, and E.S. Prusov, Strengthening Mechanisms in CoCrFeNiX0.4 (Al, Nb, Ta) High Entropy Alloys Fabricated by Powder Plasma Arc Additive Manufacturing, *Nanomaterials*, 2021, **11**(3), p 721.

41. H. Peng, S. Xie, P. Niu, Z. Zhang, T. Yuan, Z. Ren, X. Wang, Y. Zhao, and R. Li, Additive Manufacturing of Al0.3CoCrFeNi High-Entropy Alloy by Powder Feeding Laser Melting Deposition, *J. Alloys Compd.*, 2021, **862**, p 158286.

42. W.H. Liu, Z.P. Lu, J.Y. He, J.H. Luan, Z.J. Wang, B. Liu, Y. Liu, M.W. Chen, and C.T. Liu, Ductile CoCrFeNiMox High Entropy Alloys Strengthened by Hard Intermetallic Phases, *Acta Mater.*, 2016, **116**, p 332–342.

43. H. Zheng, R. Chen, G. Qin, X. Li, Y. Su, H. Ding, J. Guo, and H. Fu, Microstructure Evolution, Cu Segregation and Tensile Properties of CoCrFeNiCu High Entropy Alloy during Directional Solidification, *J. Mater. Sci. Technol.*, 2020, **38**, p 19–27.